AIAA Journal
Vol. 49, No. 1, January 2011

Time-Resolved Particle Image Velocimetry of Unsteady Shock Wave-Boundary Layer Interaction

Axel Hartmann,* P. Christian Steimle,† Michael Klaas,‡ and Wolfgang Schröder§
RWTH Aachen University, 52062 Aachen, Germany

DOI: 10.2514/1.J050635

A combination of time-resolved particle image velocimetry and unsteady pressure measurements is used to analyze the unsteady flow over an aeroelastic supercritical BAC 3-11 transport-type wing configuration in subtransonic flow. The dynamic interaction between the shock wave and turbulent separation is the essential feature of the unsteady flow causing a distinct self-induced oscillation of both the wing structure and the flowfield. Results from wind-tunnel experiments with a variation of the freestream Mach number at Reynolds numbers $\mathcal{O}(10^7\ \mathrm{m}^{-1})$ are analyzed regarding the origin and nature of the unsteady shock wave-boundary layer interaction. Time-resolved particle image velocimetry results are presented for a flow case with a weak shock and incipient separation as well as for a case with medium shock strength and full-scale trailing-edge separation. The visualization of the flowfield, which is time-resolved regarding the shock wave oscillation, demonstrates the two-fold nature of the shock wave-boundary layer interaction, on the one hand being the origin of aerodynamic unsteadiness at marginally separated flow, on the other hand damping the fluctuation level at full-scale separation.

Nomenclature

c_1 = chord of the inner pressure measuring section
c_2 = chord of the outer pressure measuring section
$\bar{c}$ = mean aerodynamic chord length
c_p = pressure coefficient
$c_{p,\mathrm{crit}}$ = critical pressure coefficient
c_∞ = velocity of sound in the freestream
f = frequency
f_s = sampling rate
M_∞ = freestream Mach number
Re_∞ = $u_\infty \bar{c}/\nu_\infty$, freestream Reynolds number based on mean aerodynamic chord
s = wing semispan
U = absolute velocity
u_∞ = freestream velocity
x = streamwise direction
x_s = shock position
y = spanwise direction
α_0 = mean incidence angle
η = y/s, normalized spanwise direction
ν_∞ = kinematic viscosity
σ = oblique shock angle
τ_p = particle-response time
ω^* = $2\pi f \bar{c}/u_\infty$, reduced frequency based on mean aerodynamic chord

I. Introduction

THE aerodynamic behavior of modern transport-type wings with supercritical airfoils and moderate sweep angles is determined by a local supersonic flowfield on the upper surface terminated by a shock with strength varying along the wing span. A highly complex and time-dependent flow pattern can exist in the direct vicinity of the wing surface with a shock-induced separation of the turbulent boundary layer in the wing trailing-edge region. The trailing-edge flow is in turn a source of unsteadiness for the shock wave and the entire wing flowfield [1]. The inviscid shock wave interacts with acoustic waves radiated from large-scale structures of a free shear layer impacting the sharp airfoil trailing edge [2]. Aeroelastic instabilities in the transonic flight regime very often occur in conjunction with this dynamic shock-boundary layer interaction generating pressure fluctuations that act on the wing structure as a time-dependent load distribution. Modern transport wings with optimized lightweight designs may exhibit a distinctive structural response to unsteady loads in the first bending–torsion mode. This dynamic fluid–structure interaction might stimulate an unstable aeroelastic flutter response of the wing structure developing a metastable structural limit cycle oscillation (LCO) due to its inherently nonlinear character [3,4]. Future transport aircraft developments require a deeper understanding of these dynamic interaction processes to take into account aeroelastic nonlinear system behavior with new methods of computational aeroelasticity [5].

With this background an extensive series of wind-tunnel tests has been conducted with a supercritical transport-type wing configuration in a transonic intermittent vacuum-storage wind tunnel at freestream Mach numbers between $M_\infty = 0.78$ and 0.92 and wing-root incidence angles between $\alpha_0 = -2$ and 3° at Reynolds numbers corresponding to the mean aerodynamic chord of the swept wing $Re_c = \mathcal{O}(10^6)$. The wing exhibits an increased degree of unsteadiness in a Mach number range between 0.82 and 0.88 at α_0 between -1 and 1° due to the time-dependent load distribution from the dynamic interaction between a medium strength shock wave and the turbulent boundary layer, eventually causing trailing-edge separation. This purely aerodynamic process promotes the exchange of kinetic energy between the flow and the wing, thereby introducing unsteadiness also to the structure [6,7]. This contribution is devoted to a further understanding of the dynamic shock–boundary layer interaction involving trailing-edge separation to characterize the role of the aerodynamic unsteadiness in the context of aeroelastic instabilities. The focus is set on the aerodynamic process since the observed aeroelastic behavior of the stiff wing model under investigation is not distinct and only a reaction to the aerodynamic forces.

Presented as Paper 2010-4826 at the 28th AIAA Applied Aerodynamics Conference, Chicago, 28 June–1 2010; received 30 April 2010; revision received 24 August 2010; accepted for publication 26 August 2010.

[*] Research Scientist, Institute of Aerodynamics, Wüllnerstraße 5a; a.hartmann@aia.rwth-aachen.de.

[†] System Engineer, Astrium Space Transportation GmbH, Airbus-Allee 1, 28199 Bremen; per-christian.steimle@astrium.eads.net.

[‡] Senior Scientist, Institute of Aerodynamics, Wüllnerstraße 5a; m.klaas@aia.rwth-aachen.de.

[§] Head of Institute of Aerodynamics, Wüllnerstraße 5a; office@aia.rwth-aachen.de.

As an extension of previous investigations focusing on unsteady flow information on the wing surface, flowfield information is presented for one representative section of the swept wing using time-resolved particle image velocimetry (TR-PIV). The results from the experimental test campaigns also can be used to assess the accuracy and validity of computational efforts regarding dynamic fluid–structure interaction.

II. Experimental Setup

The experimental investigation has been conducted in the Trisonic Wind Tunnel of the RWTH Aachen University. This facility is an intermittently working vacuum storage tunnel capable of producing flows at Mach numbers ranging from 0.4 to 3.0. For transonic flows with freestream Mach numbers below one, the tunnel is equipped with a $0.4\ \mathrm{m} \times 0.4\ \mathrm{m}$ two-dimensional adaptive test section consisting of parallel side walls and flexible upper and bottom walls to simulate unconfined flow conditions [8]. The wall contours are calculated by solving the Cauchy integral based on the time-averaged pressure distribution measured along the center line of the flexible walls [9]. Despite the three-dimensionality of the wing flow, the two-dimensional wall adaptation is assumed to be adequate due to the small size of the wing configuration used in the experiments. The total pressure and temperature of the wind tunnel are determined by the ambient conditions. Therefore, the Reynolds number depends on the Mach number and ambient temperature ranging from 1.3 to $1.6 \times 10^7\ \mathrm{m}^{-1}$ in the present experiments. The relative humidity of the flow is kept below 4% at total temperatures of about 293 K to exclude any influence on the shock wave position [10].

The acoustic environment in the wind tunnel is of major interest for the experimental simulation of dynamic fluid–structure interaction processes. For this reason, the adaptive test section is also equipped with several dynamic pressure transducers distributed along the center line of the upper and lower walls. Figure 1 displays the dominant reduced resonance frequencies $\omega^* = 2\pi f \bar{c}/u_\infty$ with affiliated power spectral power density measured along the duct center line in the empty test section for different freestream Mach numbers. The freestream chamber located downstream of the test section is identified as the main source of acoustic disturbances in the test section, since spectral powers always peak in the transducer locations closest to this area. Depending on the freestream Mach number, the acoustic disturbances contain three predominant frequencies, most likely evolving from different acoustic modes in the freestream chamber. The fluctuation power contained in the modes also depends on the Mach number. When analyzing the results of the flow measurements over the swept-wing model, the influence of the test section acoustics must be taken into account.

The wing geometry under investigation is a slender transport-type configuration with the supercritical airfoil BAC 3-11/RES/30/21 developed by the British Aerospace Corporation [11]. The back-swept wings consists of two segments with a constant leading edge sweep angle of 34° and trailing-edge sweep of 22 and 26°. It possesses a semispan of $s = 280$ mm, an aspect ratio of 7.5, and a mean aerodynamic chord of $\bar{c} = 74.3$ mm. The maximum chord of 104.35 mm is located at the wing root. The laminar–turbulent transition of the boundary layer is a significant parameter to determine the shock–boundary layer interaction. To limit the number of variables and to simulate a flow that in most respects behaves similar to a realistic high Reynolds number flow, the boundary-layer transition is fixed at a line of 5% chord with a 117 μm zigzag shaped transition strip on both wing surfaces. The effectiveness of the tripping device has been successfully verified using a shear-sensitive liquid crystalline coating during previous investigations [6].

Because of the small scale of the wind-tunnel model, it is unfeasible to incorporate the required sensor equipment into one single model. Hence, in this study two identical wind-tunnel models were investigated, each equipped with pressure transducers located at different spanwise positions. Figure 2 shows a schematic of the model geometry and the sensor positions. Both wing models are made of an identical orthotropic ultrahigh modulus carbon fiber laminate sandwich shell.

Wing model number one is equipped with 27 subminiature Entran EP-I and Kulite XCQ-080 pressure transducers incorporated in one section at a relative half span $\eta_1 = y_1/s = 0.286$, corresponding to $y_1 = 80$ mm. Because of the slenderness of the trailing edge, the pressure measuring area is limited to $0.051 \leq |x/c|_1 \leq 0.785$ on the upper and $0.085 \leq [x/c]_1 \leq 0.648$ on the lower surface of the wing, respectively. Wing model number two has 9 Kulite XCQ-080 pressure transducers installed at $\eta_2 = y_2/s = 0.714$, corresponding to $y_2 = 200$ mm, on the wing's upper surface and conventional pressure taps on the lower side for a time-averaged measurement. In this case, the pressure measuring range is limited to $0.187 \leq [x/c]_2 \leq 0.695$ on the upper and $0.134 \leq [x/c]_2 \leq 0.772$ on the lower side, respectively. For both models, each transducer is installed in closest proximity to the corresponding pressure orifice to minimize the damping and phase shift of the measured pressure signal against the actual signal on the wing surface (Fig. 3). Figure 4 shows the dynamic response of the sensor installation plotted against the reduced frequency $\omega^* = 2\pi f \bar{c}/u_\infty$ in the Mach number range of $0.8 \leq M \leq 1.4$ relevant for the flow conditions under consideration. The response function was calculated using the theory developed by Tijdeman [12] for the propagation of small harmonic pressure perturbations through tube-transducer systems. The calculations show that the response function has a very small influence on pressure fluctuations in the reduced frequency range of the flowfield oscillation that is investigated in this study.

Nevertheless, the phase shift ϕ_u/ϕ_i and the gain p_u/p_i are considered for the data evaluation, using a first order approximation of the transfer function developed by Tijdeman. In Fig. 4, the

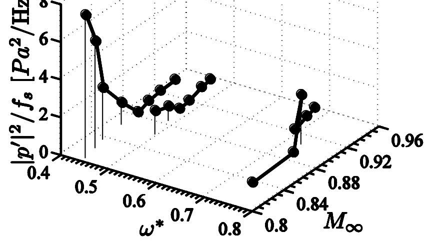

Fig. 1 Dominant resonance frequencies together with affiliated power spectral power density along the duct center line in proximity to the freestream chamber.

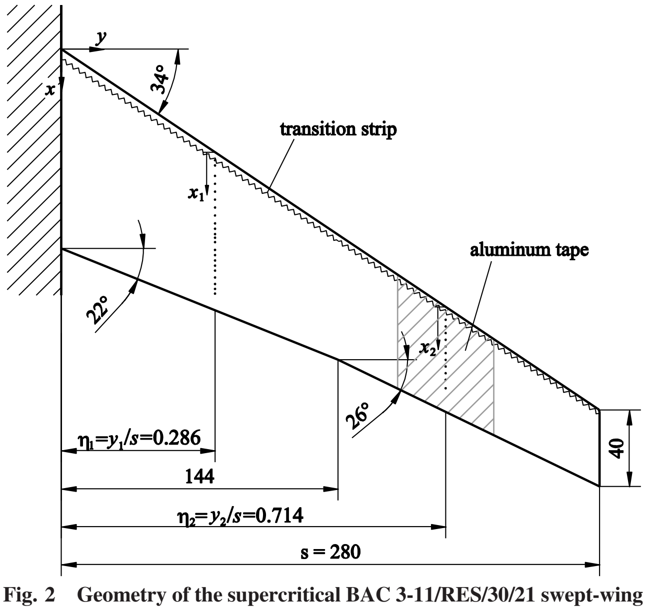

Fig. 2 Geometry of the supercritical BAC 3-11/RES/30/21 swept-wing model with pressure measuring sections at $\eta_1 = 0.286$ and $\eta_2 = 0.714$; dimensions in mm.

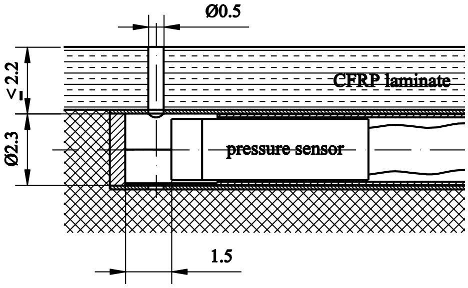

Fig. 3 Pressure transducer installation; dimensions in mm.

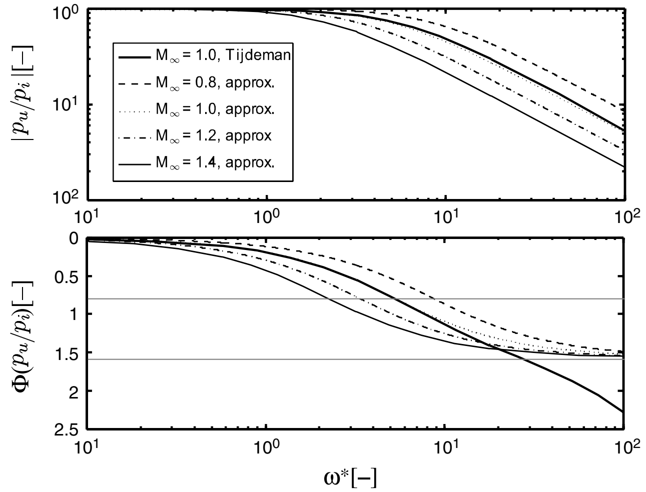

Fig. 4 Modulus and phase of sensor installation dynamic response as a function of the reduced frequency ω^* for $0.8 \leq M \leq 1.4$.

approximation of the transfer function is compared with the original function for $M = 1$ showing the validity of the approximation for the relevant frequency range of $\omega^* < 3$. The approximation allows to calculate the original pressure value p_u at the pressure orifice using Eq. (1)

$$p_u = p_i + T p_i' \tag{1}$$

with T being the time constant which is determined for each Mach number using the transfer function by Tijdeman and p_i being the pressure value at the pressure sensor. The pressure transducer signals are recorded using a data-acquisition (DAQ) system consisting of five data acquisition boards Imtec T-112 with simultaneous analog-to-digital conversion of 40 channels, 12 bit resolution, and up to 1.25 MHz sampling rate per channel. In the present experiments, a sampling rate of $f_s^{\mathrm{DAQ}} = 20$ kHz was selected. The signals are conditioned with 4-pole Butterworth low-pass filtering with 10 kHz corner frequency and hundredfold amplification with a bandwidth of 100 kHz by Endevco 136 DC-amplifiers.

In addition to unsteady pressure measurements, two-component TR-PIV with the laser light sheet positioned parallel to the incoming flow was employed to analyze the wing flowfield in the representative section $\eta_2 = 0.714$ at the test section vertical plane of symmetry. Droplets of Di-Ethyl-Hexyl-Sebacat (DEHS, CAS-No. 122-62-3) with a mean diameter of 0.6 μm were used as seeding. To achieve a homogenous seeding distribution, the seeding was added to the flow in the dry air reservoir of the wind tunnel before each test run. Using the approach of Melling [13] the particle response time τ_p can be calculated to be approximately 1.98 μs corresponding to a frequency response of $f_p = 505$ kHz.

The flow was illuminated using a Quantronix Darwin Duo 40M double-pulsed Nd:YLF laser with a wavelength of 527 nm. The repetition rate was set to 1500 Hz resulting in an energy of approximately 15 mJ per pulse. The laser light sheet was about 1 mm thick. The optical access for the laser beam was provided through an aperture in the freestream chamber of the wind tunnel downstream of the test section. Figure 5 shows an overview of the PIV setup. Using the frame-straddling technique mentioned by Raffel et al. [14], the laser pulse separation in the experiments was 2.8 μs leading to a mean particle displacement of approximately 0.85 mm, corresponding to approximately 13 pixels in the acquired flow images. The particle images were recorded with a Photron Fastcam SA-3 CMOS camera with a 1024 × 1024 pixel sized sensor capable to achieve a frame rate of 2000 Hz at full resolution. The sensor was cropped to 1024 × 512 pixels to achieve an increased recording rate of 3000 Hz leading to a sampling rate of $f_s^{\mathrm{PIV}} = 1500$ Hz. This frequency fulfills the Nyquist criterion for the expected oscillation frequencies such that we define the PIV measurements as time resolved regarding the

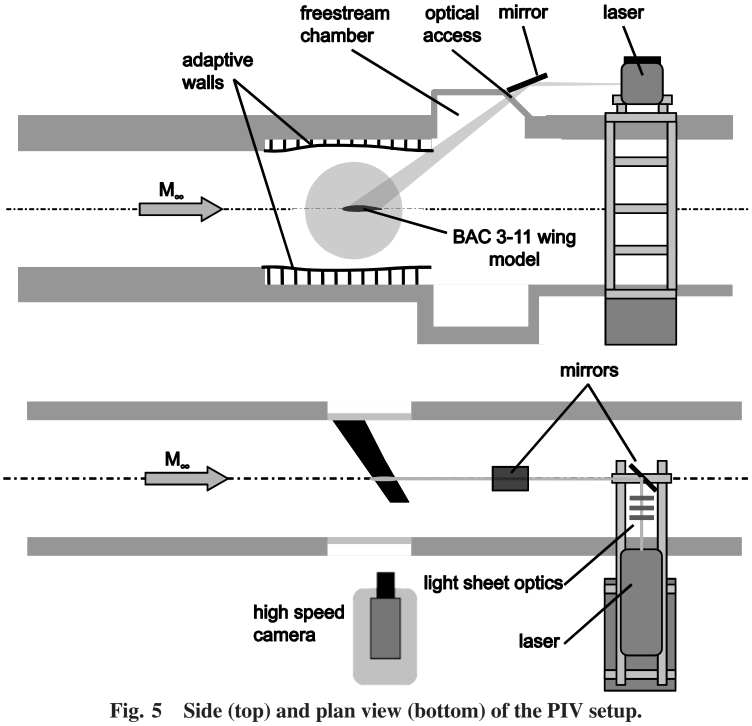

Fig. 5 Side (top) and plan view (bottom) of the PIV setup.

shock wave oscillation. An 85 mm Nikon Nikkor 1:1.8 lens together with a 20 mm intermediate ring was mounted to the camera. The optical settings result in a particle diameter of approximately 3 pixels in the recorded images. In each test run, a dataset of 2726 image pairs was acquired. The images were analyzed with ILA VidPIV software using adaptive cross-correlation with a final window size of 32×32 pixels and an overlap factor of 75%. This leads to a vector spacing of 0.53 mm. For post-processing, a window velocity and a local median filter were used to identify and remove outliers which were in the range of 1%. For the synchronization of the TR-PIV and the time-resolved pressure measurements, the exposure signal of the camera of each frame was recorded with the DAQ system used for the pressure transducer signals leading to a maximum time discrepancy of 25 μs due to the different recording rates of 3 and 20 kHz, respectively.

Exposure tests with the Nd:YLF high-speed laser with 15 mJ pulse energy showed a significant local heating of the wing surface in the area illuminated by the laser light sheet due to absorption of the carbon fiber gel coat layer. To avoid any deterioration of the surface quality and structural stiffness, a 56 mm wide and 0.2 mm thick 3M aluminum tape was incorporated into the wing surface in the area between $\eta = 0.614$ and 0.814, denoted by the shaded area in Fig. 2. The tape, which serves as a thermal barrier coating, is flush-mounted by applying it onto the surface during the lamination process to avoid any surface distortion.

III. Time-Averaged Flow Analysis

The unsteady aerodynamic flowfield at the BAC 3-11 wing has been investigated on the basis of the time-averaged aerodynamics for a wide variety of incidence angles measured at the wing root between $\alpha_0 = -2°$ and $+3°$, freestream Mach numbers between $M_\infty = 0.78$ and 0.92, and Reynolds numbers $Re_c = \mathcal{O}(10^6)$. The main feature of the transonic swept-wing flow is a weak compression shock terminating the supersonic bubble in the flowfield. Figure 6 displays the time-averaged pressure distributions in η_1 and η_2 for $M_\infty = 0.86$ and 0.92, respectively, measured with the pressure sensors incorporated in these wing sections for a constant mean angle of attack $\alpha_0 = 0°$. At $M_\infty = 0.86$ the steep pressure rise normally indicating a weak shock wave is smoothed by the time averaging, especially in the outer station η_2, indicating an unsteady shock wave motion. The unsteadiness of the flow is shown by the length of the error bars denoting the global maximum and minimum measured in each position during the testing time. It is obvious that the largest fluctuations occur around the time-averaged shock position. The large variance in the pressure signal at $[x/c]_1 = 0.151$ on the lower side is caused by the presence of a weak shock wave terminating a very small supersonic field in this area. This special feature of the BAC 3–11 pressure distribution has been described by Hillenherms [15] and cannot be analyzed further on this wind-tunnel model due to the previously described size limitations and resulting pressure orifice positions. The supersonic flow area grows with increasing freestream Mach number leading to a stronger shock that evolves closer to the trailing edge. At $M_\infty = 0.92$ a weak oblique shock is followed by a short supersonic expansion and a strong shock on the wing upper side at the inbound station. Since the leading shock is caused by a local deflection of the streamlines most likely in the vicinity of the outer boundary-layer region, the appearance of this lambda-shaped shock system marks the change from a mild to a severe interaction with the boundary layer, which is consistent with the commonly known Mach number effect on the transonic flowfield described by Seddon [16], Green [17], Adamson and Messiter [18], Délery [19], and Délery and Marvin [20].

However, the flowfield on the upper side is also characterized by a separation of the boundary layer at the trailing edge. First, the separation occurs at subcritical conditions. Then, it grows and moves

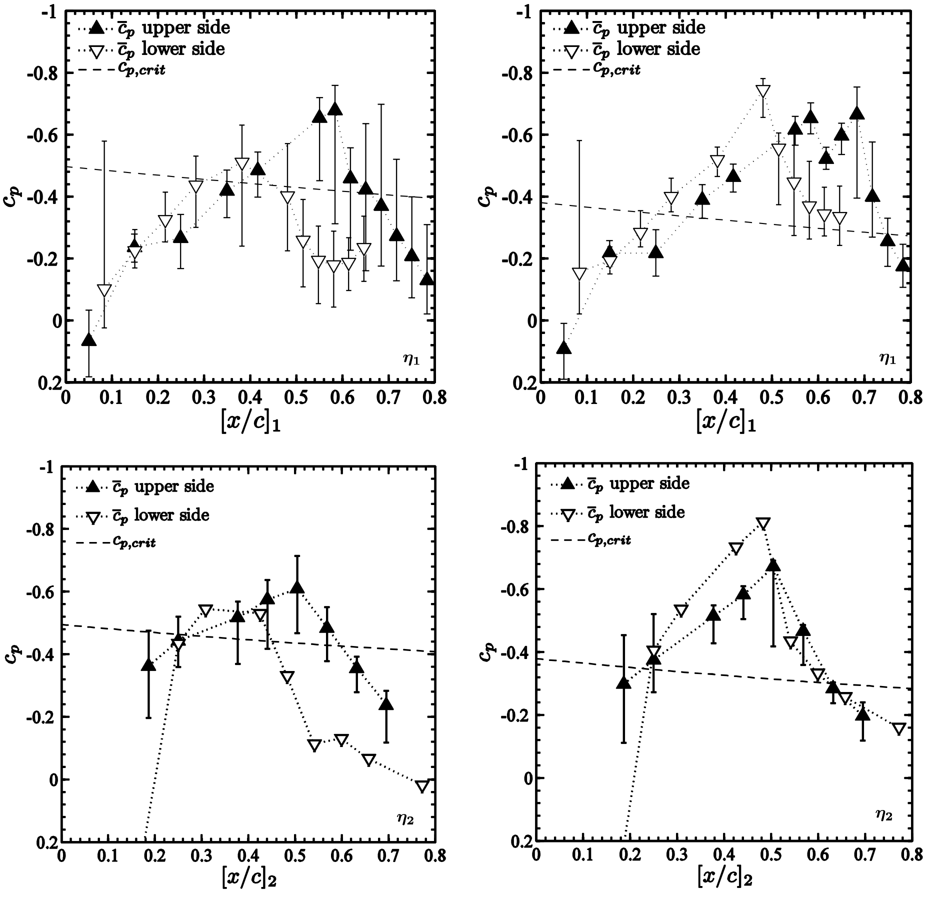

a) b)

Fig. 6 Time-averaged pressure distributions in $\eta_1 = 0.286$ and $\eta_2 = 0.714$ for a) $[\alpha_0, M_\infty] = [0°, 0.86]$ and b) $[\alpha_0, M_\infty] = [0°, 0.92]$.

upstream to finally coincide with the time-averaged shock position as soon as the shock is strong enough to induce separation. This flow development resembles the type *B*3 flow in the phenomenological description given by Pearcey et al. [21]. The oil film technique has been applied to visualize wall shear stress directions and to detect local regions of separated boundary-layer flow, as illustrated in Fig. 7. A very comprehensive review of this classic technique was given by Maltby [22]. The wing surface is coated using a mixture of oil and finely powdered luminescent pigment. During the wind-tunnel run, the oil pattern is determined by the wall shear stresses such that the dry pigment forms a streaky pattern indicating the direction of the flow close to the surface and thereby also the direction of the local skin-friction vector.

In the weak supercritical flow at $[\alpha_0, M_\infty] = [0°, 0.86]$, a significant outward deflection of skin-friction lines in the region of the pressure recovery can be observed. Near the trailing edge, the skin-friction lines eventually coincide to form a limiting streamline. This onset of trailing-edge separation is assumed to take place when the oil filaments coalesce into a quasi-common line. The development of this Pearcey *B*-type flow can be attributed to the steep pressure rise on the BAC 3–11 airfoil toward the trailing edge, as well as the thickening and skewing of the boundary layer as described by Délery [19]. Furthermore, in this low Reynolds number flow case the boundary-layer thickening due to the adverse pressure gradient is naturally much stronger than in high Reynolds number flow with naturally developed boundary-layer turbulence [18]. A schematic representation of the weak shock wave–boundary layer interaction flow is given in Fig. 8.

The appearance of the lambda shock system at a freestream Mach number of $M_\infty = 0.92$, Fig. 7b, corresponds to a full-scale separation from the shock foot to the trailing edge involving a secondary boundary-layer flow in the direction of the crosswise pressure gradient, which is indicated by the accumulation of oil in the rear part of the wing surface [23]. This accumulation also allows reconstructing the external streamlines on the basis of light streaks visible on the surface of the accumulated oil. This flow structure, which is also schematically depicted in Fig. 9, marks the performance boundary for this aerodynamic configuration due to the breakdown of lift. The flow behavior on the pressure side of the wing is similar to the upper surface, albeit with much weaker pressure gradients. Hence, the following unsteady flow analysis concentrates on the upper wing surface.

IV. Time-Resolved Flow Analysis

The time-averaged flow analysis provides a view on the global flow features, but does not give insight to the temporal development of specific flow patterns, e.g., the oscillation of the shock wave. This, for instance, was already illustrated by the smoothing effects contained in the pressure distributions caused by flow unsteadiness (Fig. 6). Nevertheless, the wing flowfield exhibits a strong streamwise oscillation in the area of the supersonic flowfield and shock wave. For the investigated spanwise station η_1, the strongest surface pressure fluctuations can be found in the region of the time-averaged shock position and in the area downstream of the shock, caused by the interaction with the boundary layer. The spectra of pressure signals from the point of incipient separation at $[\alpha_0, M_\infty] = [0°, 0.86]$ contain distinct harmonic peaks at $\omega^* = 0.42$ and 0.72 illustrating the periodic nature of the flow (Fig. 10a). As soon as the lambda shock pattern occurs, the reduced frequency of 0.72 dominates the flowfield (Fig. 10b). The spectrograms presented in Fig. 10 are representative in quality for the entire upper wing surface. Periodic shock oscillations have been investigated in several experimental and numerical studies. Brunet et al. [24] describe a pulsation of the separated area to be the origin of buffet oscillations on the OAT15A supercritical airfoil with a thickness to chord ratio of 12.5%. In his widely accepted shock buffet model, Lee [25] describes the inviscid shock interaction with upstream propagating sound waves, which are generated by the impingement of large-scale turbulent eddies on the sharp trailing edge and form a feedback loop with disturbances convected downstream, as the main buffet mechanism [26]. Shock buffet has mainly been investigated in two-dimensional flows. Finke [27] and Lee [25] measured shock buffet frequencies of $\omega^* = 0.5$ to 2.0 for the NACA 63-012 profile and $\omega^* \approx 0.5$ for the BGK No. 1 airfoil with a relative thickness of 11.8%. A reduced buffet frequency of $\omega^* = 0.55$ was measured by Schewe et al. [28] for the NLR-7301 airfoil. According to Hillenherms et al. [29,30], the BAC 3-11 airfoil exhibits a buffet frequency of $\omega^* = 0.53$ to 0.58 in the two-dimensional flow case. Hence, the measured reduced buffet frequency of $\omega^* = 0.72$ on the BAC 3-11 swept wing is in the range of that of other supercritical airfoils with a comparable thickness ratio and shock position.

Nevertheless, the shock buffet phenomenon observed on the BAC 3-11 swept wing has a different characteristic compared with shock buffet flows described in the literature. In the case of classical buffet,

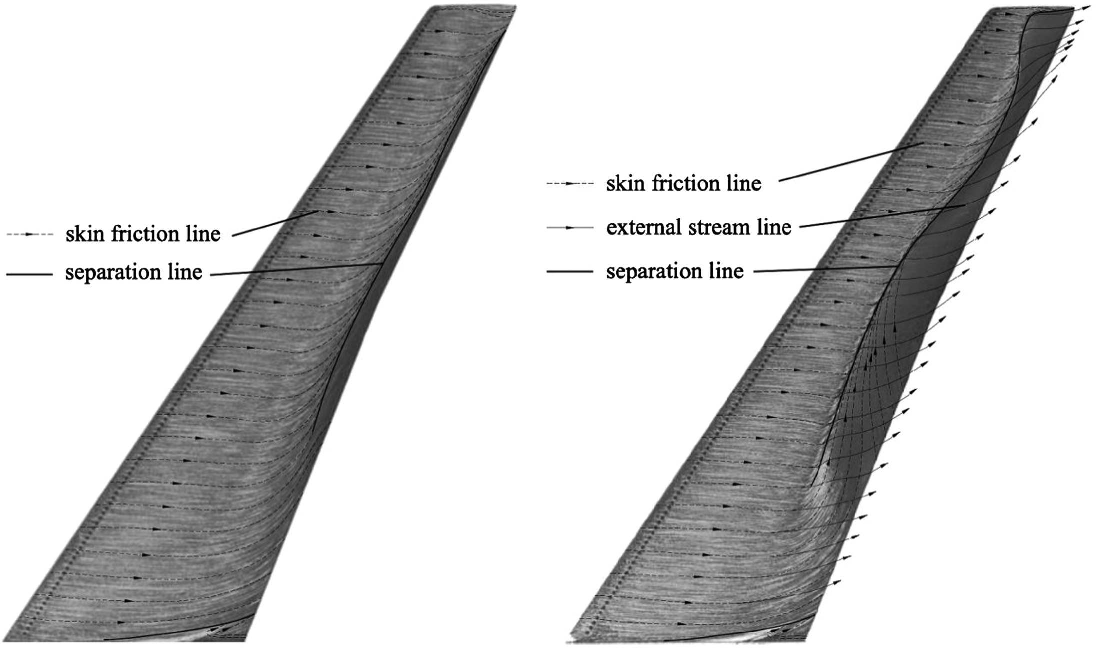

Fig. 7 Surface flow pattern on the wing upper surface, $\alpha_0 = 0.01°$: a) flow with a single shock wave and incipient separation near the trailing edge at $M_\infty = 0.86$, and b) flow with a lambda shock and shock-induced separation involving backflow at $M_\infty = 0.92$.

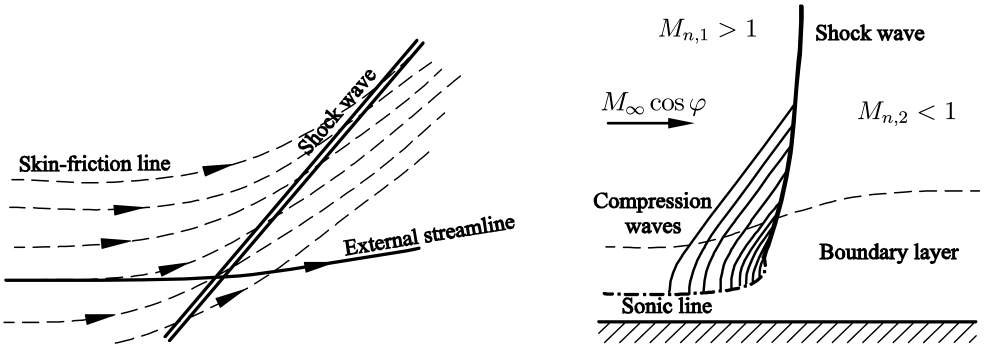

a) b)

Fig. 8 Weak transonic swept shock wave-boundary layer interaction with attached flow after Green [17] and Adamson and Messiter [18]: a) view onto the swept-wing surface, and b) view along the shock line.

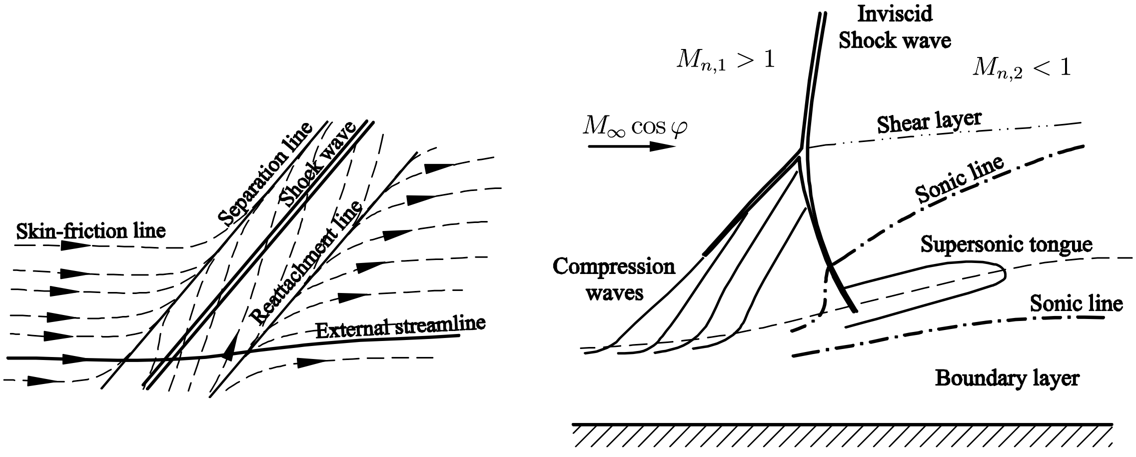

a) b)

Fig. 9 Schematic of strong transonic swept shock wave-boundary layer interaction with separation after Seddon [16] and Délery [19]: a) view onto the swept-wing surface, and b) view along the shock line.

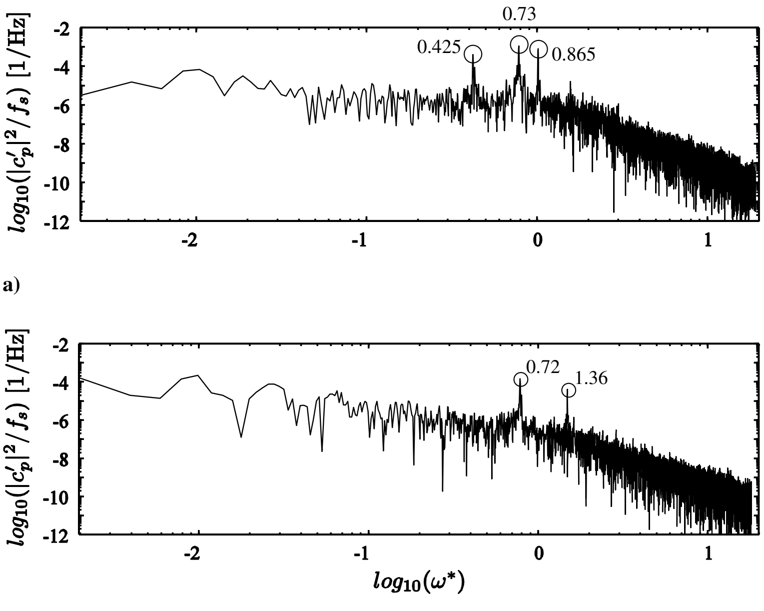

a)

b)

Fig. 10 Comparison of pressure fluctuation spectra measured in the shock region for $\eta_1 = 0.286$, $\alpha_0 = 0°$: a) $[x/c]_1 = 0.618$, $M_\infty = 0.86$, $Re_\infty = 1.09 \times 10^6$, and b) $[x/c]_1 = 0.685$, $M_\infty = 0.92$, $Re_\infty = 1.1 \times 10^6$. The reduced frequencies are also given.

the shock is strong enough to cause a fully separated flow between the shock wave-boundary layer interaction area and the trailing edge. The formation of the acoustic feed back loop can be observed at high Mach numbers and high angles of attack. In the BAC 3-11 swept-wing buffet flow considered here, the boundary layer is only slightly thickened and the shock wave is not strong enough to cause a full-scale separation during the entire cycle. The locally separated boundary-layer flow posesses a strong shear layer at the trailing edge, which generates sound waves that interact with the shock structure and amplify the unsteadiness [2,26,31]. This oscillatory shock motion, however, is only present in the range of $M_\infty = 0.84$ to 0.88 and changes to a flow with significantly lower unsteadiness at $M_\infty = 0.90$ and 0.92. At higher Mach number, the time-averaged shock foot position has shifted downstream, while the separation line appears much further upstream, induced by the stronger pressure gradient in the shock wave which dominates the inertia forces in the near-wall region, i.e., the shock wave is less sensitive to exterior perturbations. The position of the shock is fixed over time by the separation line. Hence, the flow at $M_\infty = 0.92$ exhibits a greatly reduced shock motion amplitude. The fully separated boundary layer dampens the trailing-edge noise which is why the acoustic waves interacting with the shock wave are weaker whereas the pressure gradient across the shock wave at $M_\infty = 0.92$ has increased. Thus, the remaining fluctuation power is mainly contained in the pulsation of the separated flow. The existence of a steady flow case at higher Mach numbers than the unsteady flow is also described by Xiao and Tsai [32] on an 18% thick circular arc airfoil and by Geissler [33] for the NLR 7301 airfoil in the context of numerically simulating limit cycle oscillations.

Wing deformation measurements taken during previous experiments discussed in Steimle et al. [7] justify the assumption that the shock buffet at the BAC 3-11 swept wing is a purely aerodynamic phenomenon, despite an aeroelastic coupling with the dynamic flowfield observed on the outer wing segment. The wing deformation is very small up to a relative span of about $\eta = 0.3$ with an oscillation of the local angle of attack up to 0.2° and wing bending up to 0.1% of the wing span. The spectral analysis performed with the deformation data showed that the main frequency of the wing unsteadiness is $\omega^* = 0.43$, one of the test section resonance frequencies (Fig. 1), not 0.73 or 0.72. The time-dependent deformation of the outer wing segment indeed corresponds to the flowfield oscillation in the flow case $[\alpha_0, M_\infty] = [0°, 0.86]$, while it disappears almost completely at $[\alpha_0, M_\infty] = [0°, 0.92]$.

The large fluctuations occurring in Fig. 6a near the leading edge on the lower side of the wing result from a small supersonic region terminated by a weak shock wave. The periodogram of the pressure fluctuations in this area shows the same frequencies being present here as described in Fig. 11. Thus, it is assumed that the leading edge shock wave is also sensitive to the acoustic features present in the flowfield and most likely couples with these fluctuations. The following TR-PIV measurements, however, focus on the dynamic behavior of the upper surface shock wave.

V. TR-PIV Measurements

To gain information on the velocity field, TR-PIV is used to visualize the unsteady flow around the BAC 3–11 swept-wing configuration in one measurement plane. The vertical measurement

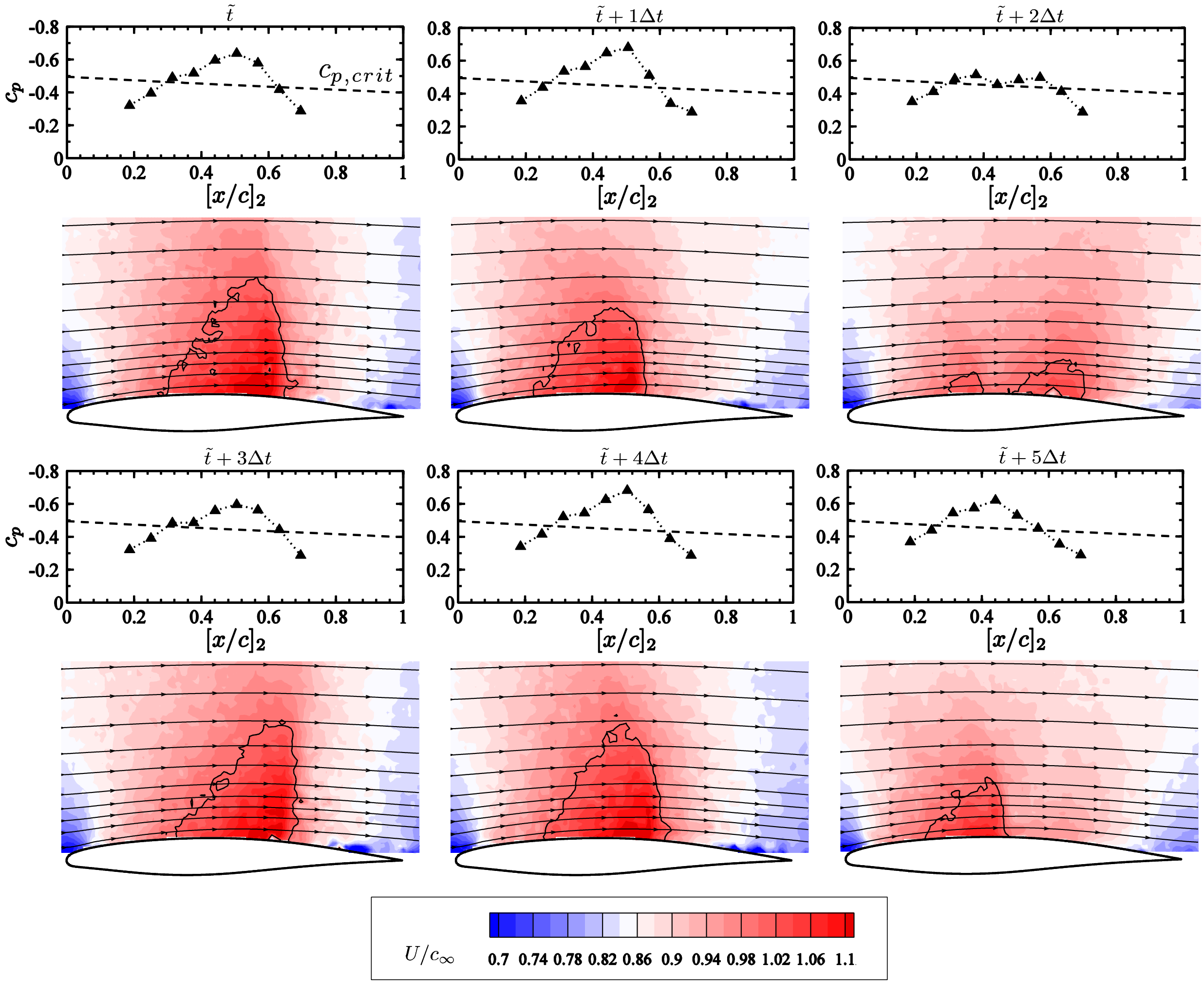

Fig. 11 Representative time sequence of synchronously measured pressure distribution and velocity field for $\eta_2 = 0.714$, $\alpha_0 = 0°$, $M_\infty = 0.86$, $Re_\infty = 1.09 \times 10^6$, time step $\Delta t = 0.67$ ms, $U/c_\infty = 1$ contour line is marked black.

plane is located along the center line of the adaptive test section and oriented in the freestream direction. Its position coincides with the $[x_2 - y_2]$ plane in the relative half-span position $\eta_2 = 0.714$. Figure 11 shows a representative time sequence of the synchronized pressure distribution and instantaneous velocity field providing almost two entire oscillation cycles of the shock wave motion. The images were acquired with $f_s^{\mathrm{PIV}} = 1500$ Hz, i.e., a time step $\Delta t = 0.67$ ms, at $[\alpha_0, M_\infty] = [0°, 0.86]$. Consistent with the results from the unsteady surface pressure measurements, a large-scale streamwise shock oscillation occurs on the upper wing surface. At time $t = \tilde{t}$, Fig. 8 shows the supersonic flow region which extends approximately from $[x/c]_2 = 0.3$ to 0.6 and is closed by a weak shock wave. One time-step later at $t = \tilde{t} + 1\Delta t$, the size of the region has decreased significantly. This shrinking is accompanied by an accelerating upstream motion of the shock wave. During this upstream shock motion, the supersonic flowfield loses its strength. The shock wave is weakened up to a point where the entire field is only slightly supersonic. At this point $t = \tilde{t} + 2\Delta t$, the cycle starts again and a new supersonic bubble develops indicated by an expansion downstream of $[x/c]_2 = 0.4$. At time step $t = \tilde{t} + 3\Delta t$, the supersonic bubble of the first cycle has completely vanished while the new supersonic bubble is fully developed comparable to that at time step $t = \tilde{t}$. In the figures, the shock wave appears as a blurred line instead of the expected sharp termination of the supersonic bubble. This is caused by the particle slip across the shock wave. With a maximum velocity difference of 85 m/s across the shock wave and the particle response time $\tau_p = 1.98$ μs, the relaxation length, which corresponds to a velocity difference of 1% between the particle and the flow, is 2.2 mm. Furthermore, the averaging effect of the PIV interrogation window method causes an additional blurring of the shock wave. That is, the measured velocity starts decreasing approximately a quarter of the size of an interrogation window of about 0.53 mm in front of the shock wave [34,35]. The resulting blurred length of 2.73 mm corresponding to 5% $[x/c]_2$ explains the relatively smooth velocity distribution behind the shock.

Quasi-harmonic large-scale shock motions were first categorized by Tijdeman [36]. An intermittent presence of the shock wave comparable to the flow behavior observed in the present study is described as Tijdeman type B shock motion. In this category, however, the shock wave disappears during part of its backward motion, while the BAC 3–11 swept-wing flow shows a disappearance of the shock close to the its most upstream position during the cycle. In Tijdeman type C motion the shock also disappears during its upstream motion, but with increasing shock strength and by propagating upstream as a sound wave into the incoming flow. The shock motion phenomenon on the BAC 3–11 swept wing is quite different from the Tijdeman description, since the supersonic region decreases in strength to cause a weakening of the shock wave during its upstream motion. The behavior primarily results from the roof top design of the BAC 3–11 wing section geometry with the local pressure coefficient increasing towards the leading edge.

The situation changes slightly at $[\alpha_0, M_\infty] = [0°, 0.92]$, since the supersonic flow is generally stronger here. Therefore, in Fig. 12, the shock wave is present during the entire oscillation cycle, while the variation in strength of the supersonic field is generally smaller. This reduced unsteadiness corresponds to the significant reduction in

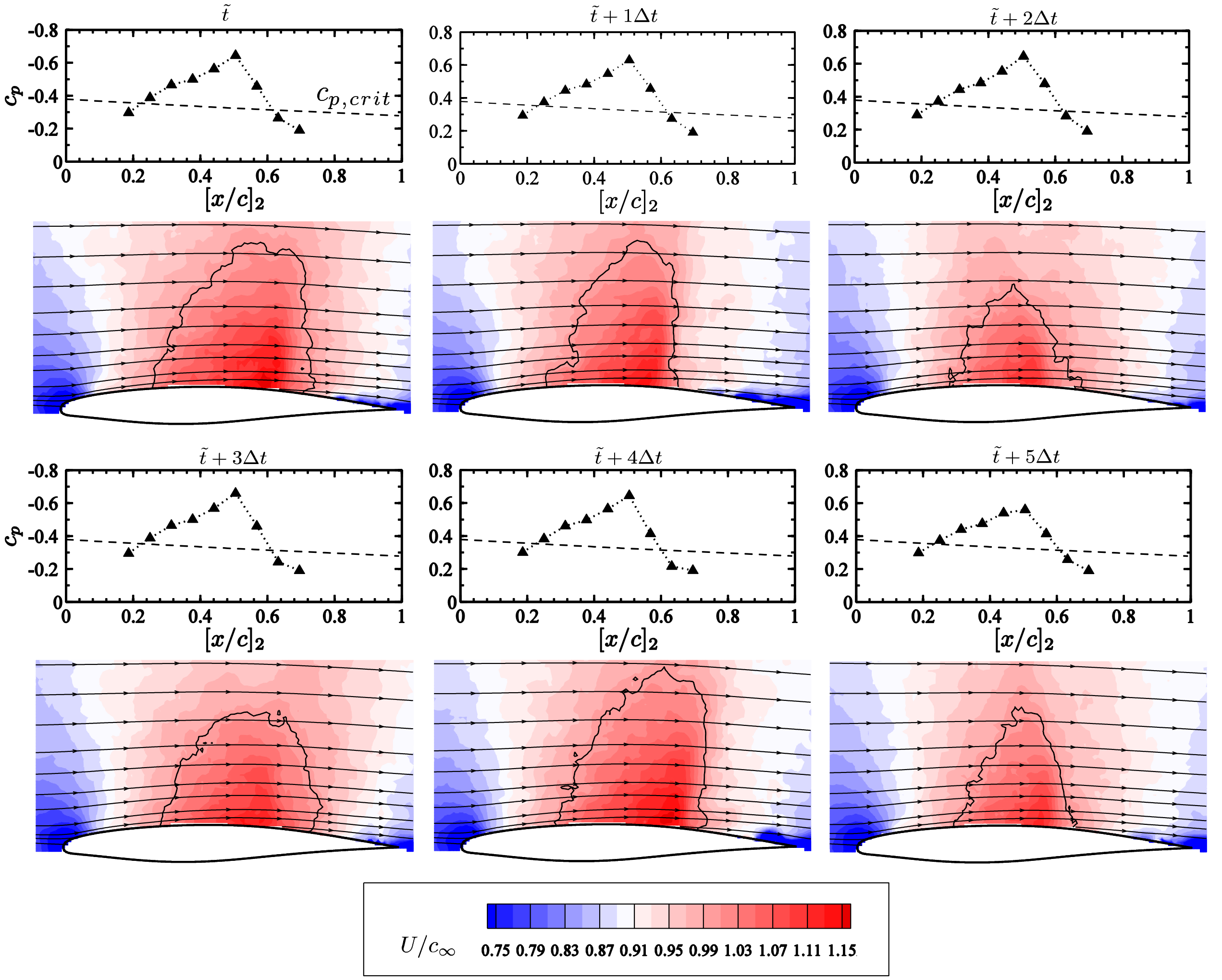

Fig. 12 Representative time-sequence of synchronously measured pressure distribution and velocity field for $\eta_2 = 0.714$, $\alpha_0 = 0°$, $M_\infty = 0.92$, $Re_\infty = 1.1 \times 10^6$, time step $\Delta t = 0.67$ ms, $U/c_\infty = 1$ contour line is marked black.

pressure fluctuation spectral power, which becomes obvious in a comparison of Figs. 10a and 10b. Compared with the flowfield at $[\alpha_0, M_\infty] = [0^\circ, 0.86]$, the velocity field at $M_\infty = 0.92$ also shows the significant difference in flow behavior regarding the trailing-edge separation. In the former case, the separation originates in closest proximity to the trailing edge (Fig. 7a). The shedding of boundary-layer structures at the sharp trailing edge is responsible for the production of sound waves travelling upstream in the subsonic region of the flowfield as was described by Brunet et al. [24], and observed by Alshabu et al. [37] on the BAC 3-11 wing section based on a numerical simulation of a buffet flow. The representative time-sequence in Fig. 8 shows that the entire flowfield is disturbed by the sound waves resulting in a continuous displacement of the shock wave into the upstream direction. The weakening of the shock wave associated with the upstream motion must be attributed to the local Mach number in the local wing flowfield which decreases continuously in the upstream direction due to the characteristic pressure distribution of the BAC 3-11 wing (Fig. 6a). In the latter case, $[\alpha_0, M_\infty] = [0^\circ, 0.92]$, the mean chordwise shock position can be found further downstream. Here, the shock is strong enough to induce a steady separation during the entire oscillation cycle. This quasi-stable correlation between the shock foot position and the separation line greatly reduces the amplitude of the shock motion. The fully separated boundary layer dampens the trailing-edge noise which is why the acoustic waves interacting with the shock wave are weaker whereas the pressure gradient across the shock wave at $M_\infty = 0.92$ has increased. Thus, the remaining fluctuation power is mainly contained in the pulsation of the separated flow. The time-series in Fig. 11 also demonstrates that the residual flow unsteadiness is solely contained in the pulsation of the large-scale separation, which causes a time-dependent deflection of the local streamlines at the outer edge of the boundary layer. Therefore, the shock oscillation is only a reaction to the change in the instantaneous downstream boundary conditions in the shock foot region.

Besides the error arising from the particle slip across the shock wave, an additional error resulting from optical distortion caused by the variation of the refractive index n across the shock wave can be estimated using a simple ray-tracing approach. Assuming that the shock wave represents a sharp interface between two media with an abrupt change of the local density of the fluid, the resulting error of the displacement of each particle can be calculated. To achieve a maximum value for such error estimation, a worst-case scenario is investigated in the following. For a maximum local Mach number of $M = 1.3$ and a shock wave angle $\sigma = 26^\circ$ measured in the experiments, the resulting density variation is $\rho_2/\rho_1 = 1.287$. Consequently, the variation of the refractive index can be calculated using the Gladstone-Dale relation to be $n_2/n_1 = 1.00004$, indicating that the influence of the optical disturbances can be neglected. Furthermore, the relatively long pulse duration of high-speed laser systems leads to an additional bias error. According to Ganapathisubramani and Clemens [38], this bias error is a function of the ratio of the pulse duration, which is determined to be $0.15\ \mu$s, to the pulse separation, being $2.8\ \mu$s and the particle displacement, such that an additional mean bias error of 0.127% has to be taken into account for the present experiments. Assuming that the accuracy of the peak detection of the PIV evaluation algorithms is in the order of 0.1 pixels [14], the overall accuracy of the velocity detection of the PIV measurements with a mean displacement of 13 pixels leads to 0.8%. The overall measurement uncertainty, besides the particle slip in the vicinity of the shock wave, then leads to about 1% applying Gaussian error propagation principles.

VI. Conclusions

Results from an experimental investigation of two different transonic flows around a BAC 3-11 swept wing with dynamic shock wave-boundary layer interaction have been presented. One flow exhibits a highly dynamic local interaction of a weak shock with a marginal trailing-edge separation due to a sound-wave/shock-wave interaction. The other flow is determined by a stronger, partly lambda shaped, shock system associated with a severe but less dynamic trailing-edge separation. For the first time, time-resolved particle image velocimetry was used to display the dynamic interaction between the oscillating shock wave and the separated flow in the rear part of the transport-type wing configuration. The results from the streamwise wing section at $\eta_2 = 0.714$ are consistent with results from previous investigations with the BAC 3-11 swept wing, which demonstrated a significant reduction in the unsteadiness of the dynamic response of the wing structure at M_∞ above 0.90. Induced by the stronger shock wave in close proximity of the marginal trailing-edge separation, a full-scale trailing-edge separation develops, the separation line being associated with a lambda-shaped shock system. The separation line itself was shown to be much less dynamic over time, thus being responsible for the reduction of flow unsteadiness. A similar conclusion in the context of aeroelastic instabilities in transonic flow has been drawn by Tichy [39] and Schewe et al. [40], who attributed the rising flutter stability limit towards higher flight Mach numbers to the occurrence of separated flow as a damping feature in the unsteady transonic wing aerodynamics.

Acknowledgments

This research was funded by the Deutsche Forschungsgemeinschaft within the Collaborative Research Center SFB 401 “Flow Modulation and Fluid-Structure Interaction at Airplane Wings” and the research project “Numerical and Experimental Analysis of Shock Oscillations at Shock Wave-Boundary Layer Interaction in Transonic Flow” (DFG SCHR 309/40-1).

References

[1] Dussauge, J-P., and Piponniau, S.,“Shock/Boundary-Layer Interactions: Possible Sources of Unsteadiness,” *Journal of Fluids and Structures*, Vol. 24, No. 8, 2008, pp. 1166–1175. doi:10.1016/j.jfluidstructs.2008.06.003

[2] Atassi, H. M., “Feedback in Separated Flows over Symmetric Airfoils,” *9th AIAA Aeroacoustics Conference*, AIAA Paper 84-2297, 1984.

[3] Bendiksen, O. O., “Role of Shock Dynamics in Transonic Flutter,” AIAA Paper 92-2121, 1992.

[4] Schewe, G., and Deyhle, H., “Experiments on Transonic Flutter of a Two-Dimensional Supercritical Wing with Emphasis on the Non-Linear Effects,” *Royal Aeronautical Society Conference on Unsteady Aerodynamics*, Royal Aeronautical Society, London, 1996.

[5] Schuster, D. M., Liu, D. D., and Huttsell, L. J., “Computational Aeroelasticity: Success, Progress, Challenge,” *Journal of Aircraft*, Vol. 40, No. 5, 2003, pp. 843–856. doi:10.2514/2.6875

[6] Steimle, P. C., Schröder, W., and Klaas, M., “Transonic Shock Buffet Interference of an Oscillating High Aspect Ratio Swept Wing,” AIAA Paper 2008-6908, 2008.

[7] Steimle, P. C., Karhoff, D.-C., Nakata, S., and Schröder, W., “Unsteady Anodized Aluminum Pressure-Sensitive Paint Measurements on a High Aspect Ratio Swept Wing in Transonic Flow,” *AIAA International Forum on Aeroelasticity and Structural Dynamics*, IFASD Paper No. 2009-122, 2009.

[8] G Romberg, H.-J., “Two-Dimensional Wall Adaption in the Transonic Wind Tunnel of the AIA,” *Experiments in Fluids*, Vol. 9, No. 43, 1990, pp. 177–180. doi:10.1007/BF00187420

[9] Amecke, J., “Direkte Berechnung von Wandinterferenzen und Wandadaption bei Zweidimensionaler Strömung in Windkanälen mit Geschlossenen Wänden,” DFVLR FB 85-62, 1985.

[10] Binion, T. W., “Potentials for Pseudo-Reynolds Number Effects, in: Reynolds Number Effects in Transonic Flow,” AGARD 303, Sec. 4, 1988.

[11] Moir, I. R. M., “Measurements on a Two-Dimensional Aerofoil with High-Lift Devices,” AGARD AR-303, 1994.

[12] Tijdeman, H., “Theoretical and Experimental Results for the Dynamic Response of Pressure Measuring Systems,” NLR TR F.238, 1965.

[13] Melling, A., “Seeding Gas Flows for Laser Anemometry, Proceedings on the Conference of Advanced Instrumentation for Aero Engine Components,” AGARD CP-399, 1986, pp. 8–1.

[14] Raffel, M., Willert, C. E., Wereley, S. T., and Kompenhans, J., *Particle Image Velocimetry: A Practical Guide*, Springer, New York, 2007.

[15] Hillenherms, H. C., “Experimental Investigation of a Supercritical Airfoil Oscillating in Pitch at Transonic Flow,” Doctoral Thesis, RWTH

Aachen University, Shaker, Germany, 2003.

[16] Seddon, J., "The Flow Produced by Interaction of a Turbulent Boundary Layer with a Normal Shock Wave of Strength Sufficient to Cause Separation," RAE TM Aero 667, 1960.

[17] Green, J. E., "Interactions Between Shock Waves and Turbulent Boundary Layers," *Progress in Aerospace Sciences*, Vol. 11, 1970, pp. 235–340.
doi:10.1016/0376-0421(70)90018-7

[18] Adamson, T. C., Jr., and Messiter, A. F., "Analysis of Two-Dimensional Interactions Between Shock Waves and Boundary Layers," *Annual Review of Fluid Mechanics*, Vol. 12, No. 1, 1980, pp. 103–138.
doi:10.1146/annurev.fl.12.010180.000535

[19] Délery, J. M., "Shock Wave/Turbulent Boundary Layer Interaction and its Control," *Progress in Aerospace Sciences*, Vol. 22, No. 4, 1985, pp. 209–280.
doi:10.1016/0376-0421(85)90001-6

[20] Délery, J., and Marvin, J. G., "Shock-Wave Boundary Layer Interactions," AGARDograph 280, 1986, pp. 90–108.

[21] Pearcey, H. H., Osborne, J., and Haines, A. B., "The Interaction Between Local Effects at the Shock and Rear Separation: A Source of Significant Scale Effects in Wind-Tunnel Tests on Aerofoils and Wings," Transonic Aerodynamics, AGARD CP-35, 1968, pp. 11-1–11-23.

[22] Maltby, R. L. (ed.), "Flow Visualization in Wind Tunnels Using Indicators," AGARDograph No. 70, 1962.

[23] Squire, L. C., "The Motion of a Thin Oil Sheet Under the Boundary Layer on a Body," AGARDograph 70, 1962, pp. 7–28.

[24] Brunet, V., Deck, S., Jacquin, L., and Molton, P., "Transonic Buffet Investigations Using Experimental and DES Techniques," Seventh ONERA-DLR Aerospace Symposium ODAS 2006, ONERA TP-2006-165, 2006.

[25] Lee, B. H. K., "Self-Sustained Shock Oscillations on Airfoils at Transonic Speeds," *Progress in Aerospace Sciences*, Vol. 37, No. 2, 2001, pp. 147–196.
doi:10.1016/S0376-0421(01)00003-3

[26] Deck, S., "Numerical Simulation of Transonic Buffet over a Supercritical Airfoil," *AIAA Journal*, Vol. 43, No. 7, 2005, pp. 1556–1566.

[27] Finke, K., "Stoßschwingungen in Schallnahen Strömungen," *VDI-Forschungsheft 580*, VDI–Verlag, Düsseldorf, Germany, 1977.

[28] Schewe, G., Knipfer, A., Mai, H., and Dietz, G., "Experimental and Numerical Investigation of Nonlinear Effects in Transonic Flutter," German Aerospace Centre Internal Rept. DLR-IB 232-2002 J 01, 2002.

[29] Hillenherms, C., Schröder, W., and Limberg, W., "Experiments on Transonic Aerodynamics about Elastically Suspended Airfoils," *Notes on Numerical Fluid Mechanics and Multidisciplinary Design*, Vol. 84, Springer, New York, 2003, pp. 351–376.

[30] Hillenherms, C., Schröder, W., and Limberg, W., "Experimental Investigation of a Pitching Airfoil in Transonic Flow," *Aerospace Science and Technology*, Vol. 8, No. 7, 2004, pp. 583.
doi:10.1016/j.ast.2004.07.001

[31] Dussauge, J.-P., Dupont, P., and Debiève, J.-F., "Unsteadiness in Shock Wave Boundary Layer Interactions with Separation," *Aerospace Science and Technology*, Vol. 10, 2006, pp. 85–91.
doi:10.1016/j.ast.2005.09.006

[32] Xiao, Q., and Tsai, H. M., "Numerical Study of Transonic Buffet on a Supercritical Airfoil," *AIAA Journal*, Vol. 44, No. 3, 2006, pp. 620–628.
doi:10.2514/1.16658

[33] Geissler, W., "Numerical Study of Buffet and Transonic Flutter on the NLR 7301 Airfoil," *Aerospace Science and Technology*, Vol. 7, No. 7, 2003, pp. 540–550.
doi:10.1016/S1270-9638(03)00065-8

[34] Raffel, M., and Kost, F., "Investigation of Aerodynamic Effects of Coolant Ejection at the Trailing Edge of a Turbine Blade Model by PIV and Pressure Measurements," *Experiments in Fluids*, Vol. 24, Nos. 5–6, 1998, pp. 447–461.
doi:10.1007/s003480050194

[35] Scarano, F., and Haertig, J., "Application of Non-Isotropic Resolution PIV in Supersonic and Hypersonic Flows," *5th International Symposium on Particle Image Velocimetry*, Busan, Korea, 2003.

[36] Tijdeman, H., "Investigation on the Transonic Flow around Oscillating Airfoils," Ph.D. Thesis, NLR TR 77090 U, Technical Univ. Delft, The Netherlands, 1977.

[37] Alshabu, A., Olivier, H., and Klioutchnikov, I., "Investigation of Upstream Moving Pressure Waves on a Supercritical Airfoil," *Aerospace Science and Technology*, Vol. 10, No. 6, 2006, pp. 465–473.
doi:10.1016/j.ast.2006.04.003

[38] Ganapathisubramani, H. B., and Clemens, N. T., "Effect of Laser Pulse Duration on Particle Image Velocimetry," *AIAA Journal*, Vol. 44, No. 6, 2006, pp. 1368–1370.

[39] Tichy, L., "Transsonische Strömungen an Einem Schwingenden Profil und Deren Einfluß auf die Flattergrenze," Dissertation, Technische Universität München, DLR Fachbericht 92-08, 1992.

[40] Schewe, G., Mai, H., and Dietz, G., "Nonlinear Effects in Transonic Flutter with Emphasis on Manifestations of Limit Cycle Oscillations," *Journal of Fluids and Structures*, Vol. 18, No. 1, 2003, pp. 3–22.
doi:10.1016/S0889-9746(03)00085-9

D. Papamoschou
Associate Editor